A New Digital Terrain Model of the Huygens Landing Site on Saturn's Largest Moon, Titan

C Daudon, A Lucas, S Rodriguez, S Jacquemoud, A Escalante lópez, B Grieger, E Howington-kraus, E Karkoschka, R Kirk, J. T. Perron, et al.

Earth and Space Science

RESEARCH ARTICLE
10.1029/2020EA001127

A New Digital Terrain Model of the Huygens Landing Site on Saturn's Largest Moon, Titan

C. Daudon[1], A. Lucas[1], S. Rodriguez[1], S. Jacquemoud[1], A. Escalante López[2], B. Grieger[2], E. Howington-Kraus[3], E. Karkoschka[4], R. L. Kirk[3], J. T. Perron[5], J. M. Soderblom[5], and M. Costa[2]

[1]Université de Paris, Institut de Physique du Globe de Paris, CNRS, Paris, France, [2]RHEA System for ESA, European Space Astronomy Centre, Madrid, Spain, [3]Astrogeology Science Center, U.S. Geological Survey, Flagstaff, AZ, USA, [4]Lunar and Planetary Laboratory, Tucson, AZ, USA, [5]Department of Earth, Atmospheric and Planetary Sciences, Massachusetts Institute of Technology, Cambridge, MA, USA

Key Points:
- We create a new digital terrain model (DTM) of the Huygens landing site that offers the best available resolution of river valleys on Titan
- The complexity of the data set requires a tailor-made reconstruction procedure that is detailed
- The workflow uses reprocessed Huygens/DISR images and an automated shape-from-motion algorithm to improve an earlier DTM

Supporting Information:
- Supporting Information S1

Correspondence to:
C. Daudon,
daudon@ipgp.fr

Citation:
Daudon, C., Lucas, A., Rodriguez, S., Jacquemoud, S., Escalante López, A., Grieger, B., et al. (2020). A new digital terrain model of the Huygens landing site on Saturn's largest moon, Titan. *Earth and Space Science*, *7*, e2020EA001127. https://doi.org/10.1029/2020EA001127

Received 3 FEB 2020
Accepted 9 AUG 2020
Accepted article online 12 AUG 2020

Abstract River valleys have been observed on Titan at all latitudes by the Cassini-Huygens mission. Just like water on Earth, liquid methane carves into the substrate to form a complex network of rivers, particularly stunning in the images acquired near the equator by the Huygens probe. To better understand the processes at work that form these landscapes, one needs an accurate digital terrain model (DTM) of this region. The first and to date the only existing DTM of the Huygens landing site was produced by the U.S. Geological Survey (USGS) from high-resolution images acquired by the DISR (Descent Imager/Spectral Radiometer) cameras on board the Huygens probe and using the SOCET SET photogrammetric software. However, this DTM displays inconsistencies, primarily due to nonoptimal viewing geometries and to the poor quality of the original data, unsuitable for photogrammetric reconstruction. We investigate a new approach, benefiting from a recent reprocessing of the DISR images correcting both the radiometric and geometric distortions. For the DTM reconstruction, we use MicMac, a photogrammetry software based on automatic open-source shape-from-motion algorithms. To overcome challenges such as data quality and image complexity (unusual geometric configuration), we developed a specific pipeline that we detailed and documented in this article. In particular, we take advantage of geomorphic considerations to assess ambiguity on the internal calibration and the global orientation of the stereo model. Besides the novelty in this approach, the resulting DTM obtained offers the best spatial sampling of Titan's surface available and a significant improvement over the previous results.

1. Introduction

After 13 years of observations by the Cassini-Huygens mission (Cassini orbiter and Huygens lander), Titan, Saturn's largest moon, turned out to be a unique body in the solar system. Singularly similar to the Earth, its surface displays morphologies that look familiar to us: drainage basins and river systems (Burr et al., 2006, 2013; Collins, 2005; Lorenz & Lunine, 1996; Lorenz et al., 2008), lakes and seas (Cornet et al., 2012; Hayes et al., 2008; Lopes et al., 2007; Porco et al., 2005; Stofan et al., 2007), dune fields (Barnes et al., 2008; Lorenz et al., 2006; Radebaugh et al., 2008; Rodriguez et al., 2014), and incised mountains (Aharonson et al., 2014; Barnes et al., 2007; Lorenz et al., 2007; Radebaugh et al., 2007; J. M. Soderblom et al., 2010).

Titan has a thick atmosphere mainly composed of nitrogen and methane that are ionized and dissociated in the upper atmosphere by ultraviolet photons and the associated photoelectrons (Galand et al., 2010; Yung et al., 1984). These complex reactions produce aerosols, which end up as solid sediments on the icy surface. They have a strong impact on surface energy budget and on the climate of Titan, consequently playing an active role on landscape formation. The pressure (1.5 bar) and temperature (94 K) prevailing on the surface of Titan induce a methane cycle similar to Earth's water cycle. It allows evaporation, condensation into clouds, and rainfalls (Atreya et al., 2006; Hayes et al., 2018; Lunine & Atreya, 2008). This cycle also induces a range of processes, such as fluvial erosion, that shape landscapes (Jaumann et al., 2008; Lorenz & Lunine, 1996). Similar to erosion by water on Earth, liquid methane carves into the surface to form river valleys clearly visible at all latitudes in the images acquired by the Cassini-Huygens mission

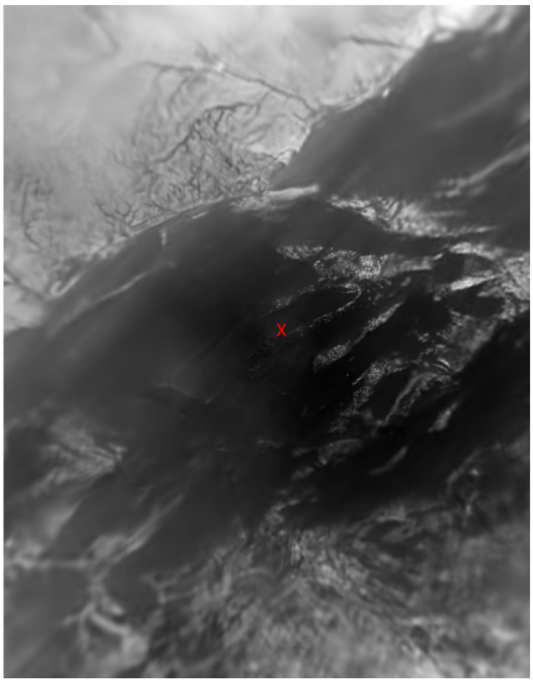

Figure 1. Medium-altitude mosaic (250 m to 50 km) (E. Karkoschka, https://pds-atmospheres.nmsu.edu/PDS/data/hpdisr_0001/EXTRAS/MOSAICS/MOSIACS_PNG/). The red cross in the center of the image indicates the Huygens landing site.

(Langhans et al., 2012; Lopes et al., 2016). Rivers are particularly striking in the high-resolution images (i.e., a few tens of meters) acquired near the equator (167.664°E, −10.573°N) by the Huygens Descent Imager/Spectral Radiometer (DISR) instrument, when the Huygens probe landed on Titan on January 2005. Although liquid methane has not been identified, these images reveal dark features that are interpreted as dry fluvial channels (Perron et al., 2006; Tomasko et al., 2005), where liquid may have flowed in recent history and carved the bright highland region before draining the materials into the flat dark lowlands (Figure 1). The fact that these lowlands are spectrally compatible with a slight enrichment in water ice (Barnes et al., 2007b; Brossier et al., 2018; Rodriguez et al., 2006) and the observation of rounded, icy pebbles on the ground confirm this hypothesis. These pebbles were most likely transported and deposited downstream by the rivers (Keller et al., 2008; Tomasko et al., 2005).

However, the geological processes that sculpt these rivers and their link with climate at different latitudes are still open questions. As far as the equatorial regions are concerned, several studies based on image analysis hypothesized that the rivers observed at the Huygens landing site were mechanically incised from methane precipitation-runoff processes (Aharonson et al., 2014; Perron et al., 2006; Tomasko et al., 2005). Other studies further investigated these questions by comparing 3-D morphologies simulated by landscape evolution models with the local topography retrieved from the observations of the Huygens mission (Black et al., 2012; Tewelde et al., 2013). The frequency and intensity of equatorial precipitations, which control the formation and the evolution of these rivers, and therefore the age and the current activity of these landforms, are still largely unconstrained. A way to better understand the ongoing processes in this region is thus to build an accurate digital terrain model (DTM) of the Huygens probe landing site where there are the most resolved images of Titan surface. These images have been acquired by the DISR panchromatic cameras (with a spectral range going from 660 to 1,000 nm) during the descent of the Huygens probe. They were not intended for photogrammetric reconstruction but, thanks to the wind, the probe slightly swung allowing to acquire a few pairs of images with sufficient overlap. From these images, the U.S. Geological Survey (USGS) produced a DTM of the bright region incised by rivers near the landing site of Huygens using SOCET SET©, a commercial photogrammetry software. A first version of this DTM was presented in Tomasko et al. (2005), and the process of reconstruction was partly explained by L. A. Soderblom, Tomasko, et al. (2007) and Archinal et al. (2006). For clarity, this DTM will be referred as USGS-DTM in the following. As it was the only one showing Titan's rivers at a decameter resolution, it has been used in many studies (Black et al., 2012; Jaumann et al., 2008; L. A. Soderblom, Kirk, et al., 2007; Tewelde et al., 2013; Tomasko et al., 2005). Although the USGS-DTM is the best topographic model of the Huygens landing area produced to date, it is limited by the quality of the data and the mapping technology. Their authors tried to improve the accuracy by revising the geometric calibration of the DISR cameras, and they attempted to quantify the precision of the measured elevations (Archinal et al., 2006). These efforts to make, assess, and fully document the additional DTMs were unfortunately cut short by the end of Huygens mission funding.

At that time, all of the source data products needed to build DISR DTMs were in preliminary and rapidly changing states. Radiometric and cosmetic (compression artifact removal and sharpening) processing of the images had not been finalized, so the versions of the images used were later superseded and never archived. As noted by Archinal et al. (2006), the cameras were geometrically recalibrated, but their optical parameters never published. Only a preliminary estimate of the Huygens descent trajectory was available to constrain the camera position for each image, with no prior information about camera pointing. The version of the Huygens trajectory archived in the PDS (Planetary Data System) differs from both the version used as input for the USGS-DTM and the photogrammetrically adjusted camera positions. As a result, the geometry of stereopairs could only be reconstructed with limited accuracy, so that elevations are relative rather than absolute. The lack of a priori position and pointing information also meant that there was no way to identify potential stereopairs more efficiently than by visual examination of the images. This limited both the effort to

Table 1
Characteristics of the Images Selected to Reconstruct the IPGP-DTM

Image ID	414	420	450	462	471	541	553	601
Camera	HRI	HRI	HRI	HRI	HRI	MRI	MRI	MRI
Altitude (km)	16.7	16.7	14.5	14.1	12.8	10.1	9.9	7.4
Average ground sampling (m/px)	17.8	17.8	15.5	15.1	13.7	21.4	21.0	15.0

map additional areas and the ability to improve the quality of a DTM by using multiple overlapping images. Finally, attempts to use the automatic image matching module of SOCET SET were unsuccessful because of the relatively low signal-to-noise level and the extremely small size of the DISR images. The USGS-DTM was thus generated by visually identifying remarkable features. This process restricts the resolution of the DTM because areas that do not contain mappable features have been filled by interpolation. Unfortunately, the available output from SOCET SET includes only the resulting gridded DTM, not the record of the features actually measured. For all these reasons, it is difficult, or even impossible, to reproduce the USGS-DTM as is and to assess the impact of changing individual steps of the processing, because most of the input parameters are unavailable in their original form.

There are other reasons for concern that impact the use of the USGS-DTM to interpret the morphology and the geology of the landing site. The dome shape of the bright highlands is particularly inconsistent with the drainage patterns observed in the images. Such a topography should lead to a radial shape of the river network, while a dendritic one is observed. Moreover, because of this dome shape, some rivers flow in the wrong direction (upstream), whereas most studies suggest a runoff from the bright highlands to the dark lowlands, which are considered as a dry riverbed or lakebed (Burr et al., 2013; Perron et al., 2006). These discrepancies may result from the difficulty of controlling the images (i.e., improving the knowledge of camera positions and pointing given the limited starting data that were available) described above. As a result, it is likely that the overall USGS-DTM is not properly leveled, and because it was produced from overlapping stereopairs, the apparent dome could be the result of different leveling errors on the two sides. The limited resolution of the manually produced DTM also confounds efforts to assess the complete geometry of the stream courses.

All theses reasons led us to revisit the topographic mapping of the Huygens site. In addition to investigate the apparent errors in the USGS-DTM, we will take advantage of recent advances in the processing of the Huygens data and the stereoanalysis softwares to generate a significantly improved DTM and, ultimately, to map a larger area of the landing site with additional stereopairs. We will also fully document our data sources, methodology, and final products so that others can reproduce or extend our work.

Since the USGS-DTM realization, recent postprocessing of the DISR images were performed (Figure 3) to correct both for the radiometric and geometric distortions (Karkoschka & Schröder, 2016; Karkoschka et al., 2007). A reestimate of the navigation data (SPICE kernels) is also available (Charles, 1996; ESA SPICE Service, 2019). The new DTM, hereafter called the IPGP-DTM, was built using MicMac, a free and open-source photogrammetry software (Bretar et al., 2013; Pierrot-Deseilligny & Clery, 2011; Pierrot-Deseilligny & Paparoditis, 2006). MicMac applies a shape-from-motion (SfM) algorithm to generate large point clouds. To manipulate the Huygens images, which were originally not intended for photogrammetric reconstruction, a tailor-made reconstruction procedure was required. The strategy detailed in this article can be applied to any target with unusual photogrammetric conditions, for instance, when the parallax between images is very small. In section 2, we present the DISR instrument and the new image processing. Section 3 details the method used to build the IPGP-DTM, and in section 4 we compare the (new) IPGP-DTM to the (old) USGS-DTM and validate it against morphometric arguments.

2. New Processing of the DISR/Huygens Images

2.1. The DISR Instrument and Images: Nominal Processing

The region of interest has been imaged by the DISR instrument, which observed the surface of Titan with unprecedented resolution near the equator (Table 1). The DISR downward-looking instruments include three panchromatic cameras (Table 2): the Side-Looking Imager (SLI), the Medium-Resolution Imager (MRI), and the High-Resolution Imager (HRI). The light is transmitted from the lens system of each camera

Table 2
Characteristics of the DISR Downward-Looking Instruments: High-Resolution Imager (HRI), Medium-Resolution Imager (MRI), and Side-Looking Imager (SLI) (Lebreton et al., 2005; Tomasko et al., 2002, 2003)

Camera	Focal length (mm)	Sensor size (mm)	Zenith range (°)	Size (pixel)
SLI	6.262	2.94 × 5.88	45.2–96	128 × 256
MRI	10.841	4.05 × 5.88	15.8–46.3	176 × 256
HRI	21.463	3.68 × 5.88	6.5–21.5	160 × 256

Note. The focal length is provided by Archinal et al. (2006), and the sensor size can be deduced from the size of the individual pixels/photosites found on the ESA PSA website (https://sci.esa.int/cassini-huygens/31193-instruments/?fbodylongid=734).

to a shared charge-coupled device (CCD) through optical fiber bundles. The optical fiber ribbons are contained in independent conduits; therefore, each camera can be treated as a separate sensor throughout the DTM reconstruction pipeline (Figure 2).

Half of the DISR images are missing due to the loss of one of the two radio transmission channels in the probe receiver on board the orbiter (Karkoschka & Schröder, 2016; Lebreton et al., 2005; Tomasko et al., 2005). Nevertheless, about 300 images of the surface of Titan are available at a resolution ranging from ~3 mm to ~1 km. The aerosol haze was too thick to discern the surface in the first 25 min of the descent of Huygens, but the landscape started to be visible at an altitude of about 50 km.

Before their transmission to Earth, onboard processing operations including flat-field correction, dark subtraction, and replacement of bad pixels were carried out. Unfortunately, image artifacts have been introduced on this occasion. The most significant comes from the use of prelaunch, embedded algorithms dedicated to the flat-field correction. The displacement of the fiber optic bundle during launch, entry, and descent greatly changed the response of the flat fields (Figure 2). The application of prelaunch reduction algorithms consequently ended in a significant degradation of the overall quality of the images (DISR Data User's Guide, https://pds-atmospheres.nmsu.edu/PDS/data/hpdisr_0001/DOCUMENT/DISR_SUPPORTING_DOCUMENTS/DISR_DATA_USERS_GUIDE/DISR_DATA_USERS_GUIDE_3.PDF).

Another issue concerns the irreversible image compression before transmission to Earth. The images were first converted from 12 bits to 8 bits using a look-up table similar to a square root transformation. Then they were compressed on board with a discrete cosine transform (DCT) algorithm. This transform is equivalent to a JPEG compression, a lossy operation that discards small valued coefficients. Although the loss was lower than the noise in most images, it was significant in some images with a high information content (Karkoschka & Schröder, 2016).

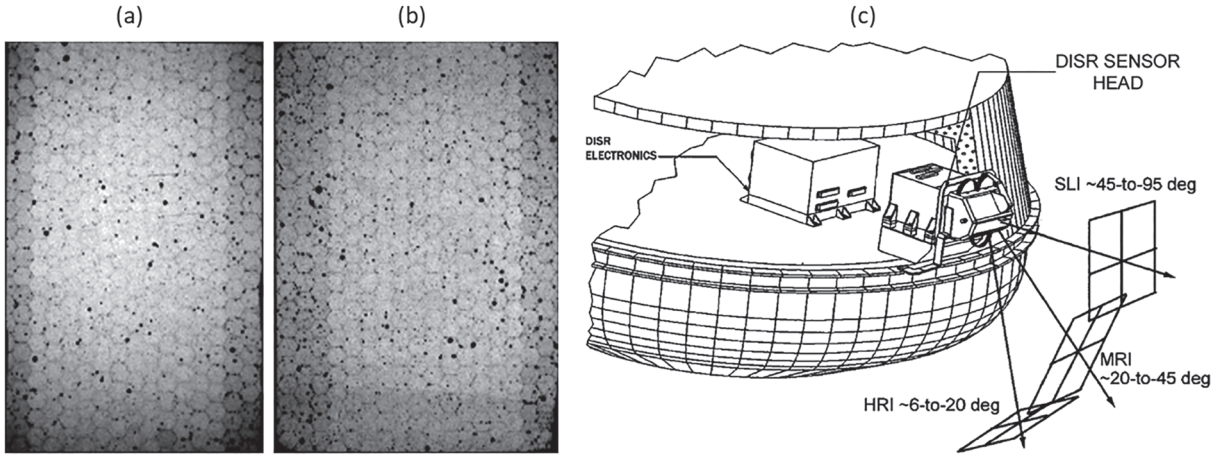

Figure 2. Flat field of (a) the HRI camera and (b) the MRI camera, showing the response of the instrument to uniform illumination. The "chicken wire" pattern is due to the seams between individual fiber optic strands (DISR Data User's Guide). (c) The DISR instrument looking out of the Huygens probe. The three viewing directions of the imagers (HRI, MRI, and SLI) are shown (University of Arizona).

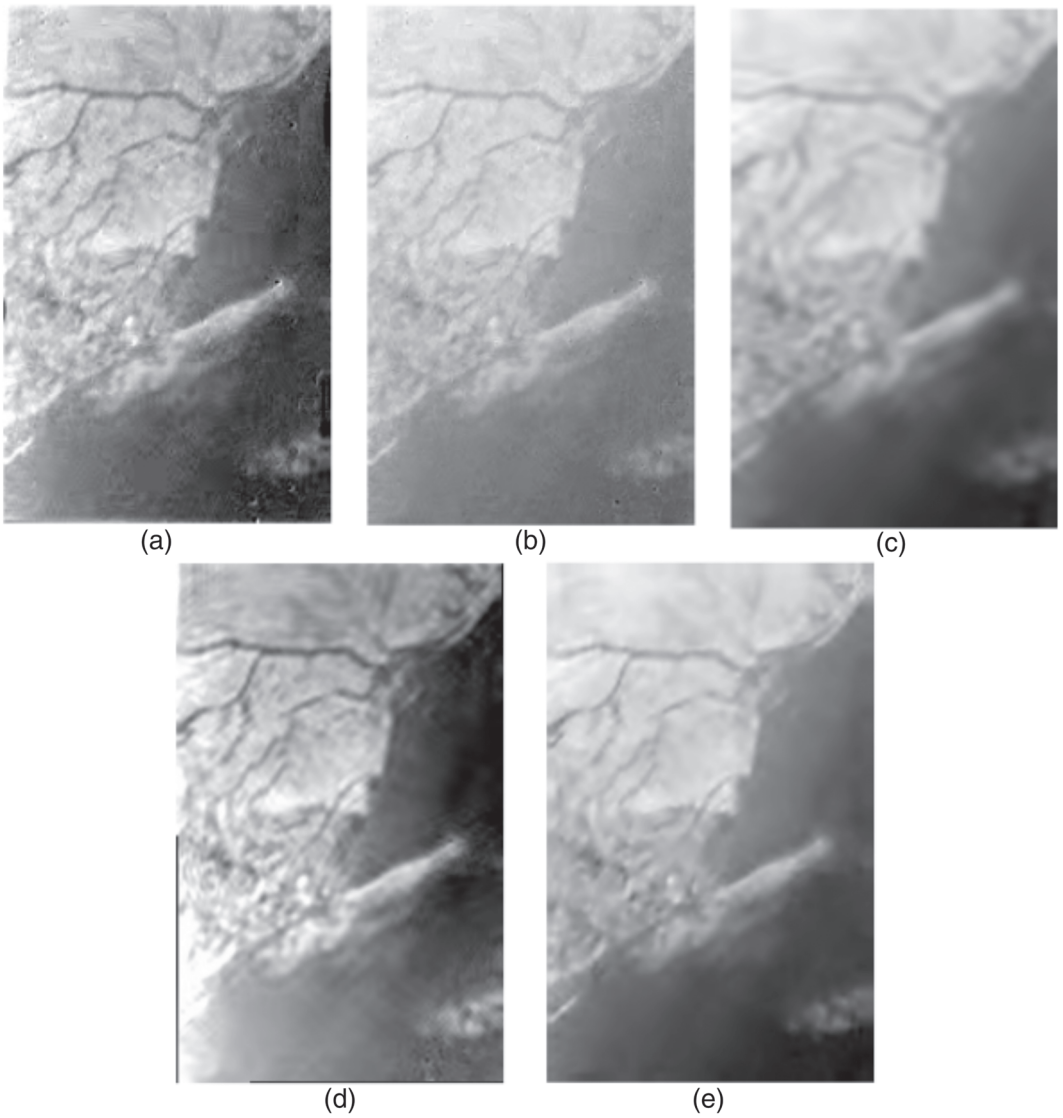

Figure 3. Comparison of five generations of images (Image #414): (a) Raw image photometrically stretched. (b) Image corrected for flat-field, dark, bad pixels, and electronic shutter effect. (c) Image further processed to remove compression-induced artifacts and to adjust for geometric distortions. (d) Image with undocumented postprocessing used to produce the USGS-DTM. (e) Enhanced image obtained with the new processing and used to produce the IPGP-DTM (Karkoschka & Schröder, 2016).

2.2. Decompression and Postprocessing

The DISR images are decompressed and postprocessed after transmission to Earth: (1) Their photometric stretch is square root expanded to restore the 12-bit depth, (2) they are flat-field corrected to eliminate the photometric distortions of the cameras, (3) the dark current is removed using the camera model at the exposure temperature, (4) the electronic shutter effect caused by data clocking is compensated for, (5) the images are further flat fielded to remove artifacts seen at the highest altitudes (flat, homogeneous upper atmosphere), (6) the stretch is enhanced to increase the dynamics, and (7) the bad pixels are replaced by their neighbors. The images have also been processed so as to remove compression artifacts and adjusted for geometric distortions of the camera optics and refraction from the atmosphere (see supporting information Figure S1).

In an early version of the DISR data set, the decompressed pixel values were rounded to the nearest integer before applying an inverse square root, which led to a significant information loss. The new image processing has corrected these errors and removed the residual radiometric artifacts (e.g., Karkoschka, 2016;

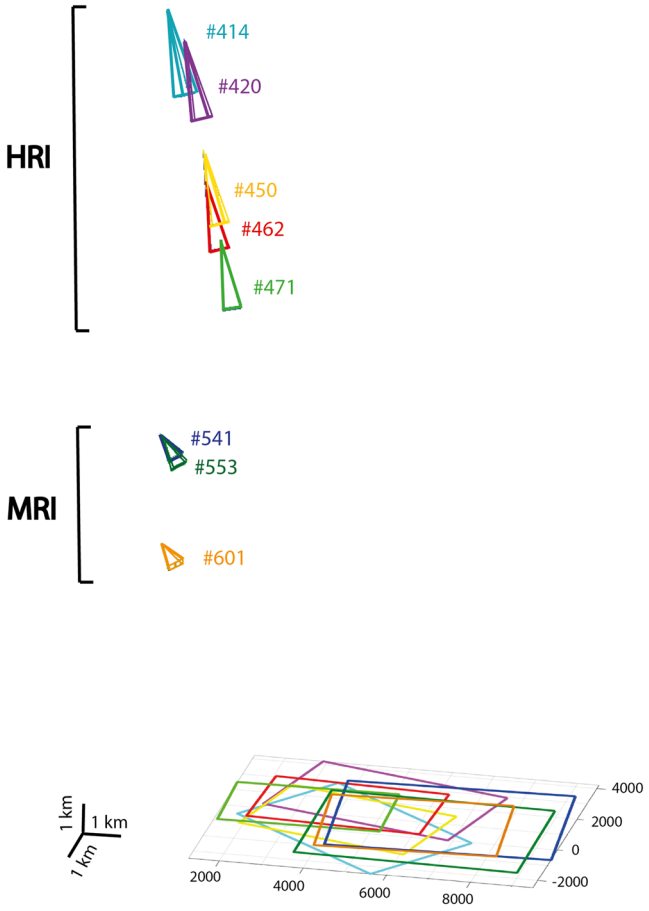

Figure 4. Position and orientation of the HRI and MRI cameras at the shooting time of the eight selected images, extracted from the SPICE kernels (ESA SPICE Service, 2019), and images footprint. The focal lengths are enlarged by a factor of 300, and the coordinates are expressed in meters in a local tangent frame (Appendix A).

Karkoschka & Schröder, 2016; Karkoschka et al., 2007). Indeed, the standard decompression scheme produced images that consist of certain spatial frequencies in each 16 × 16 pixel block with noticeable boundaries between adjacent blocks. In many images, artifacts generated by the compression were more apparent than real features on the surface of Titan. That problem was fixed by smoothing high spatial frequencies (Karkoschka et al., 2007). The method was recently improved by Karkoschka and Schröder (2016) who use a lower degree of smoothing so the new images display significant radiometric and geometric differences compared to those used to build the USGS-DTM (L. A. Soderblom, Tomasko, et al., 2007; Tomasko et al., 2005). Note that the latter have been also postprocessed, but the method used is not documented. The images with the most up-to-date corrections are used to reconstruct the IPGP-DTM (Figure 3e).

3. Building the IPGP-DTM

3.1. Image Selection and Navigation Data

Eight stereoscopic images (#414, #420, #450, #462, #471, #541, #553, and #601) were selected for the photogrammetric reconstruction (see supporting information Figure S2) of the IPGP-DTM owing to their optimal areas of overlap and resolutions (Table 1). Half of them were used to generate the USGS-DTM (#414, #450, #553, and #601). We only processed those acquired by the HRI and MRI cameras because the coarser surface resolution and the higher emission angles of the SLI camera were not suitable for DTM reconstruction. The HRI camera acquired images with the largest focal length and from the highest altitude compared to the MRI camera (Figure 4). Such a configuration enabled us to use the two cameras because the average ground sampling is similar for both of them (Table 1).

Due to the presence of a thick haze layer in Titan's atmosphere, the images acquired between 50- and 30-km altitudes were too blurry for photogrammetric reconstruction. Below, the wind was weak (4 m/s) and the descent almost straight with a slight lateral drift (Karkoschka et al., 2007; Tomasko et al., 2005). Such a geometry is definitely not optimal for photogrammetric reconstruction because of low image overlap, variable pixel size, and very small B/H ratio (the distance B between two camera point of views compared to the altitude H) (Figure 4).

The position and orientation of the Huygens probe during the descent were first computed by the Huygens Descent Trajectory Working Group (DTWG). The positions are given with an uncertainty of the order of 0.24° in longitude, 0.17° in latitude, and ranging from 0.05 to 8.3 km in altitude. They have been reestimated by the ESA SPICE Service. The Spacecraft Ephemeris Kernel (SPK) containing the position and velocity of the probe during the descent were generated using data from the DTWG (Kazeminejad & Atkinson, 2004; Kazeminejad et al., 2011). They were computed by numerical integration of the equations of motion, providing the position of the probe in spherical coordinates with respect to the Titan centered fixed frame, together with the altitude derivative with time. The finite difference method provided good results for the velocity vectors thanks to the high time resolution of the data. Finally, a polynomial interpolation was performed between datapoints for the creation of the kernel.

For the generation of the Camera Kernel (CK) that contains the attitude of the probe, thus the pointing direction of the cameras, the body angles of the probe were reconstructed with the geometry derived from the DISR images provided by Karkoschka et al. (2007). Lastly, in order to smooth the evolution of the data points, the spin rate from housekeeping data was introduced in the calculations and used to write another CK, which implements the actual angular rate with the exact attitude of the probe at each moment of shooting. The Frame Kernel (FK) and Instrument Kernel (IK) that complement the CK have been defined according to the standard fixed frames and parameters of the probe provided by the Huygens User manual.

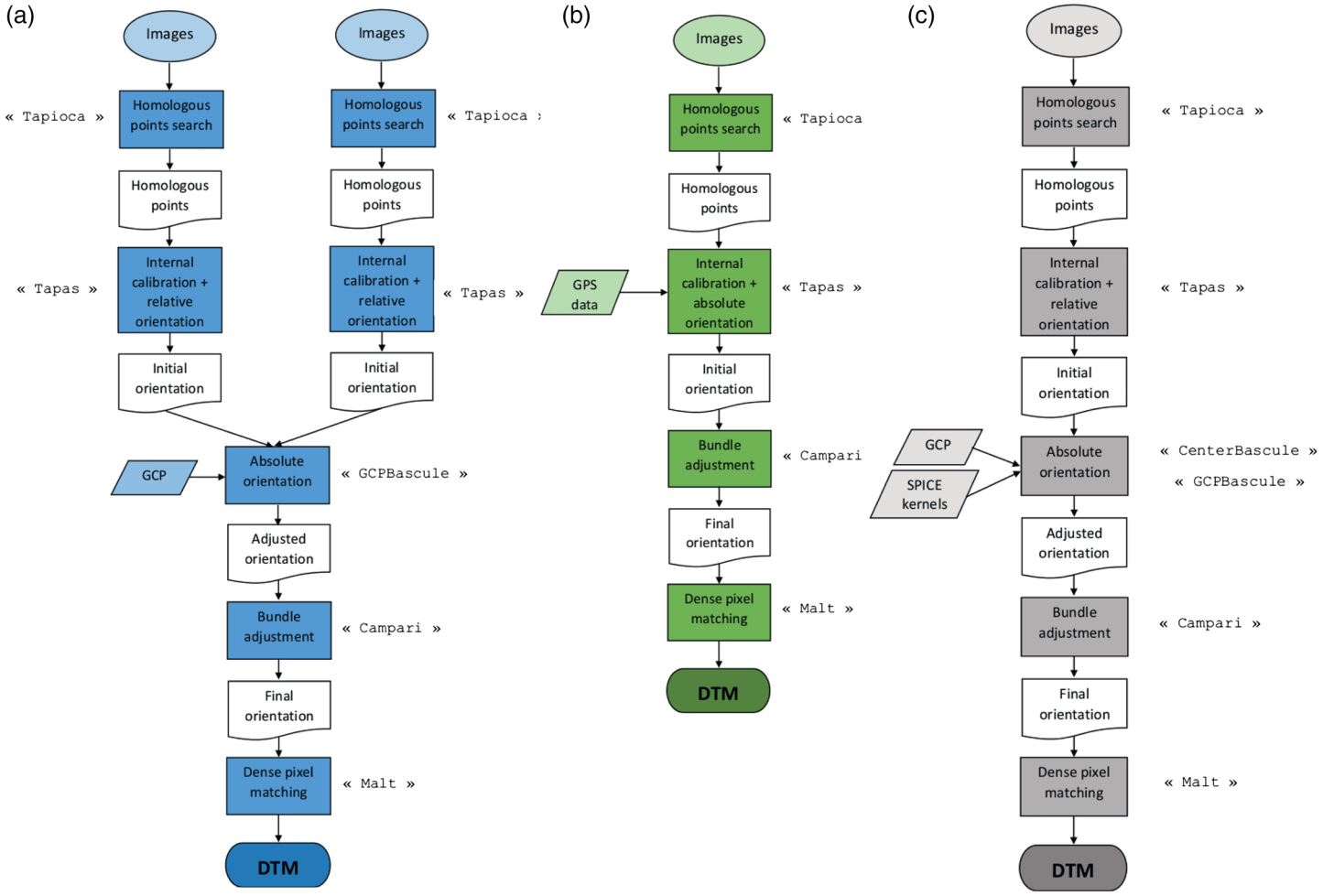

Figure 5. Diagrams of a typical reconstruction workflow for (a) an "architectural" scenario and (b) a "drone" scenario. (c) Summary diagram of the specific IPGP-DTM extraction workflow. GCP refers to ground control points. The MicMac commands are noted in quotation marks along with the corresponding steps in the workflows.

3.2. IPGP-DTM Construction Using MicMac

The construction of the IPGP-DTM was carried out with MicMac, a free and open-source photogrammetry suite developed by IGN (Institut National de l'Information Géographique et Forestière) and ENSG (Ecole Nationale des Sciences Géographiques) (Bretar et al., 2013; Pierrot-Deseilligny & Clery, 2011; Pierrot-Deseilligny & Paparoditis, 2006). We selected MicMac because it allows a large degree of freedom in the sensor models and in the 3-D reconstruction strategies, which makes it a relevant tool for our application. Since the images and the geometries of acquisition are not optimal, it is important to control the parameters at each stage of the reconstruction. MicMac also incorporates a correlator that proved to be more reliable and robust than in other photogrammetry softwares (Rosu et al., 2015). Another important issue is that any user can reproduce the IPGP-DTM.

Regarding our particular data set, we developed a specific workflow. Indeed, we are in a particular case at a crossroads between two typical scenarios:

- the "architectural" scenario, which tries to reconstruct a complex structure and usually deals with different focal lengths of the same camera in order to capture all the details of the studied structure.
- the "drone" scenario, where images are acquired by a short focal length camera on board a drone with inaccurate GPS data.

These two scenarios can be easily handled by MicMac following a classical pipeline (Figure 5). Yet our data set is a mix of the two scenarios with different focal lengths and imprecise navigation data. Moreover, the

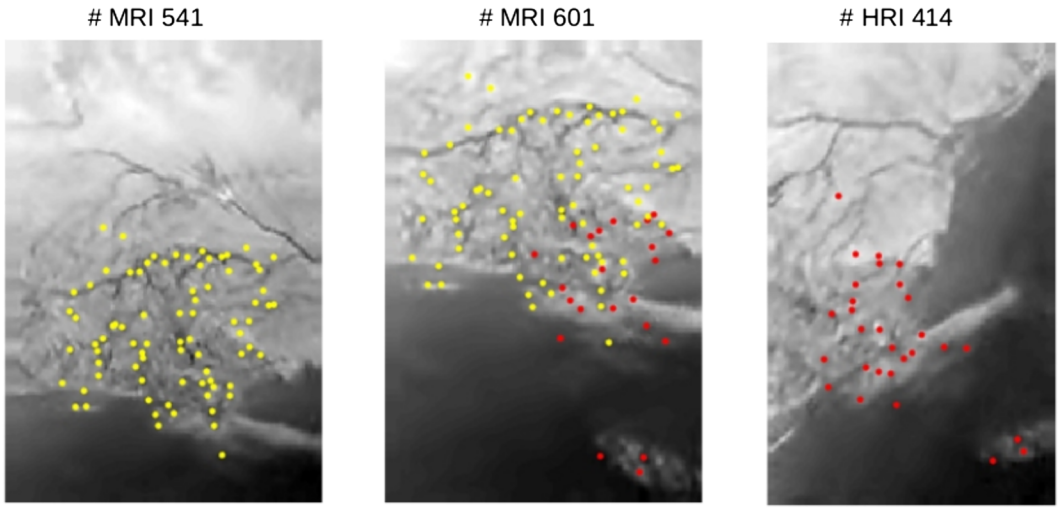

Figure 6. Example of homologous points found between two image pairs by the SIFT correlator of MicMac: in yellow, between #MRI601 and #MRI541 (79 points) and in red, between #MRI601 and #HRI414 (29 points).

parallax of our images is small, and we are working with two different cameras. We therefore could not apply an existing workflow and had to develop an entirely new procedure for this particular data set (Figure 5). This workflow can be extended to any case where the camera configuration is complex (low parallax and overlap, imprecise navigation data, no ground control points [GCP], etc.).

Batch commands can be run from a command line, and the three main steps of the photogrammetric reconstruction (homologous points search, absolute orientation, and depth map construction) are divided into six substeps corresponding to different commands (Figure 5). The entire reconstruction process is fast (i.e., about 5 min on a dual socket Xeon workstation) on small images (five images 256 × 160 pixels and three images 256 × 176 pixels).

3.2.1. Homologous Points Search

The first step consists in applying the SIFT correlation algorithm to find homologous points between each image pairs (Lowe, 2004). MicMac applies SfM techniques (Bretar et al., 2013); that is, it works with multi-view stereo images. To maximize the number of points, we look for the homologous points of each pixel of the images without degrading the resolution of the images. Depending on the image pair (Figure 6), between 10 and 80 points are detected. Their high density and their homogeneous distribution are a prerequisite for an optimal DTM reconstruction. Considering the low contrast and low texture of the images, especially in the dark area, the number and distribution of homologous points are satisfying. In comparison, we also tried to search homologous point with SOCET SET and found only three points with these new images.

3.2.2. Orientation and Position of the Cameras

The second step aims to find the orientation and the position of the cameras as the images were acquired. It is the most delicate stage. Indeed, although the SPICE kernels predicting the Huygens probe position and orientation during the descent have been recently recomputed, the altitude and the attitude are determined with an accuracy larger than 0.24° in longitude and 0.17° in latitude, which is inadequate for photogrammetry reconstruction. Thus, given the poor quality of the images and the low constraints on the camera position and orientation, this stage must be performed carefully.

The absolute orientation of the sensor is generally found by MicMac in two stages. The first is the internal calibration that computes a relative orientation using only the images; it provides an initial estimate of the position and the orientation of the optical center in any reference frame, allowing a reestimation of the sensor parameters such as the focal length, the boresight position and orientation, and the distortion parameters. Then, one can provide the absolute orientation that consists in replacing the nongeoreferenced data computed by the relative orientation by the georeferenced data. In our case, four substeps are required to achieve the final orientation: one for the relative orientation, two for the absolute orientation, and one for the orientation refinement. At the end, the absolute positions and orientations of the cameras at the time of shooting are provided for the eight selected DISR images in a local tangent frame (Appendix A).

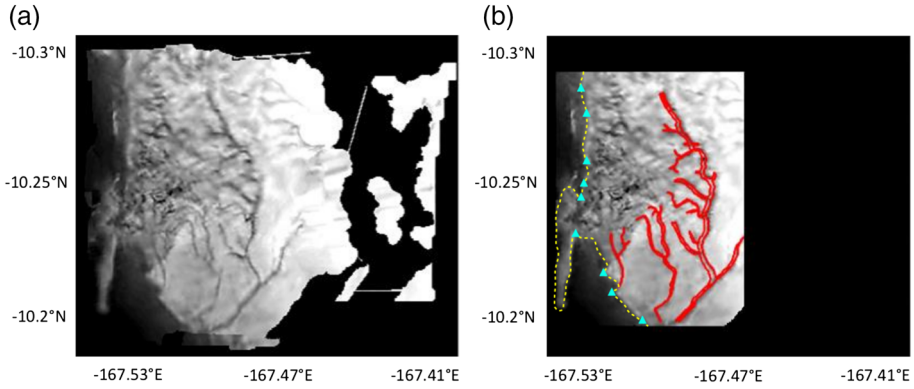

Figure 7. (a) Orthorectified mosaic of the selected DISR image (i.e., projected mosaic accounting for the relief) build by MicMac. (b) Orthorectified image masked according to the correlation score and the EP value (see section 3.2.4). The shoreline is depicted by a yellow dotted line, the ground control points are represented by cyan triangles, and the major rivers are drawn as red lines. The coordinates (in m) are in a local tangent frame (Appendix A).

After several tests, we decided to discard the internal calibration during the relative orientation because reestimating these parameters using poor-quality images is unreliable. We consequently trusted the preexisting calibration of the sensors using the focal lengths and the sensor size found in the DISR User Guide. If not, this step does not converge. However, a first estimation of the position of the optical center and the orientation of the optical axis is carried out during this stage using the images. This step is not essential to compute the final orientation but necessary for MicMac to calculate the absolute orientation.

Then, the absolute orientation is determined in two steps. The first one aims to compensate between the relative orientation and the positions provided by the SPICE kernels, which means that it applies a 3-D homothety (rotation, translation, and scaling) to the preexisting relative orientation. This first step is necessary in order to switch to field coordinates because no preexisting cartography is at our disposal. The second one consists of fixing GCP, the field coordinates of which are known, in order to externally constrain the global orientation. Even if the absolute field coordinates of the site are unknown, some GCPs can be defined with a priori knowledge of the landscape. For instance, several studies asserted that the boundary between the dark and bright areas observed in the Huygens landing site (Figure 7) was a remnant shoreline (e.g., Perron et al., 2006; L. A. Soderblom, Tomasko, et al., 2007; Tomasko et al., 2005). We therefore chose to set GCP on the shoreline by imposing on them the same relative elevation (i.e., the shoreline being an equipotential). This second step allows to constrain and improve the orientation, as shown by the projected orthoimages taking into account this new orientation and position of the cameras (Figure 8).

Finally, we performed a bundle adjustment to refine the position and the orientation of the cameras by unlocking the distortion parameters. This technique allows to simultaneously reestimate the coordinates of the 3-D points (i.e., the GCP) and the camera positions. To do so, it minimizes the root-mean-square error

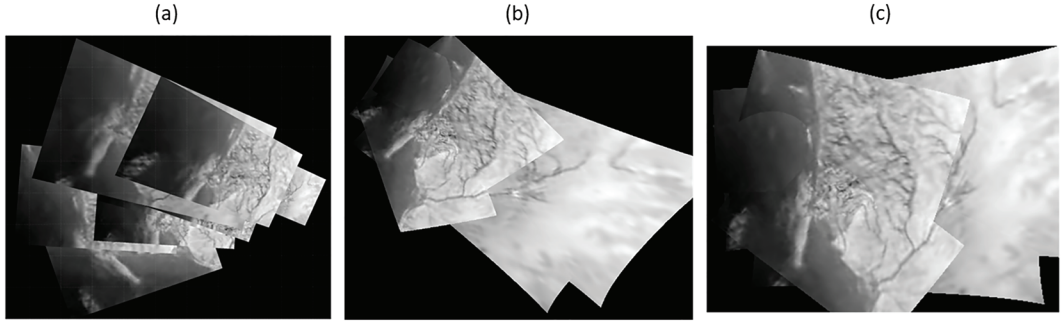

Figure 8. (a) Orthorectified mosaic obtained by projecting DISR images using the positions and orientations from the SPICE kernels only, (b) orthorectified mosaic obtained from the position and orientation of the cameras computed through the pipeline presented in this work but without using GCP (see Figure 5), and (c) orthorectified mosaic obtained with the final position and orientation computed through the entire pipeline (and thus, using GCP).

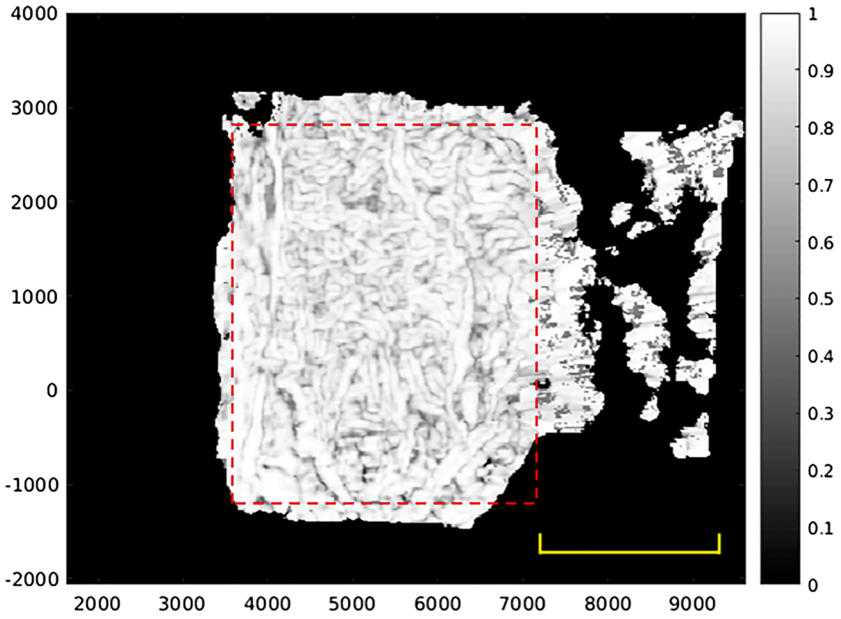

Figure 9. Correlation map showing the best correlation score for each pixel (its corresponding normalized histogram is in supporting information Figure S4). The yellow horizontal bar indicates the region with the worst correlation scores, where most of the pixels are seen with an emission angle greater than 35°. The red dotted line delimits the region used for Figures 11 and 12. The coordinates (in m) are in a local tangent frame.

between the points detected in the images and the reprojections obtained from the camera positions (Triggs et al., 1999). We do not unlock the other parameters (focal length and detector size) because we do not have enough constraints to reevaluate them. This is partly due to the small number of tie points because of the small size of the images and to the fact that we deal with two different cameras, which increases the number of unknown parameters. If we unlock all the parameters, the algorithm does not converge. The result of this compensation gives the final position and orientation in the local tangent frame. To estimate the quality of this orientation, we projected the pixels to the ground and verified that the structures in the images were continuous (Figure 8).

3.2.3. Depth Map Computation

Once the final positions and orientations of the cameras have been retrieved, an automatic matching technique allows to compute a dense matching point cloud and to derive a DTM. This step consists in matching each pixel of each pair of images. We consider each pixel along the epipolar line and calculate its similarity with the point of the second image. Since direct comparison of the images radiometry is complicated, for instance, because of the noise, the similarity is computed with a correlation coefficient. This is done for each pair of images, which means that for each pixel of the DTM, two to eight images might have contributed to its matching. To optimize the matching, we performed a sensitivity analysis by changing the value of the input parameters:

- the resolution used in the final stage of the matching (parameter ZoomF). In our case, given the small size of the images, we used them at full resolution; otherwise, all the details would have been lost;
- the size of the correlation window (parameter SzW). To partially overcome the noise problem, the correlation is usually calculated on pixel neighborhood (also called thumbnail) and not on pixels alone. The larger the thumbnail, the smoother the DTM;
- the quantification step (parameter ZPas). The thumbnail is moved along the epipolar line with a given step, defined by this parameter;
- the regularization factor (parameter Regul) used for the computation of the correlation coefficient.

We converged on a set of parameters (see supporting information section S1) that introduced as little noise as possible while keeping as much information as possible (see Appendix B). The output of this optimized automatic matching provides the final depth map, where the coordinate and elevation are expressed

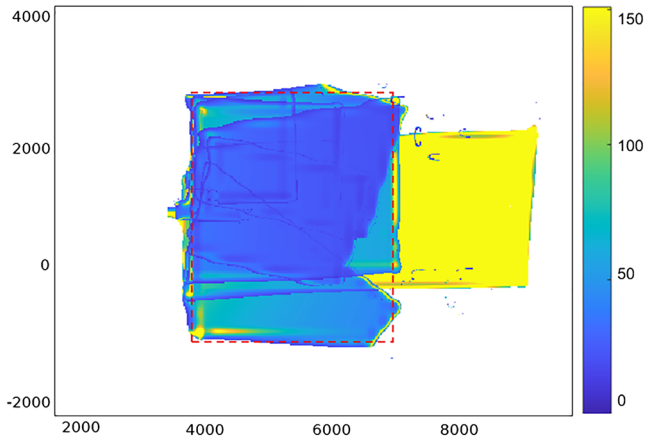

Figure 10. Expected vertical precision map (in m) for each pixel of the overlapping area. When the emission angles of two images are almost equal, EP tends toward infinity (put in white color). The color bar is thresholded up to 150 m, and the red dotted line delimits the region used for Figure 11 and Figure 12. The coordinates (in m) are in a local tangent frame.

in pixels. If the pixel size is known, then we can generate a final DTM expressed in meters, referenced in the local tangent frame. The resulting DTM named IPGP-DTM is displayed in section 3.3 and 4.

Sixty-three percent of the pixels are matched in the region with stereo coverage, which means a correlation score greater than 0. The failing areas correspond to camera emission angles greater than 30° (see supporting information Figure S3). Otherwise, the correlation score is very good with 92% of the pixels having values greater than 0.7 (Figure 9). This is a major improvement of our reconstruction compared to the USGS-DTM for which the automatic correlation failed, requesting an intensive manual editing of the DTM (L. A. Soderblom, Tomasko, et al., 2007).

3.2.4. DTM Uncertainties

DTM uncertainties are hardly ever provided by commercial softwares because they are difficult to estimate, especially when the "ground truth" is missing. Usually, the DTM accuracy is quantified by the root-mean-square error (RMSE) that computes the difference between the DTM values and other values of the same area coming from a more accurate source (e.g., Global Navigation Satellite System [GNSS] reference points). When such ancillary data are missing, the problem is rarely addressed. Thus, DTM uncertainties, other than those related to the instrument, are barely provided. In our case, they can be only estimated through the expected vertical precision (also called *EP*) for each stereo pair (Kirk et al., 2003). *EP* is based on the geometry of acquisition and the image resolution so it is an estimate of the best achievable accuracy.

$$EP = \rho * \frac{GSD}{p/h} \tag{1}$$

where

- ρ is the accuracy (expressed in pixels) with which features can be matched between the images (i.e., the root-mean-square [RMS] stereomatching error).
- *GSD* is the ground sample distance (i.e., spacing of pixels on the ground).
- p/h is the parallax-to-height ratio describing the convergence geometry of the stereo pair. It can be computed in two ways:
  $p/h = B/H$ where H is the flying height and B the distance between the cameras at the time of shooting (also called "stereo base").
  $p/h = |tan(e_1) \pm tan(e_2)|$, where e_1 and e_2 are the two emission angles. The + sign is used if the target is viewed from opposite sides, and the − sign if it is viewed from the same side.

In our case, ρ accounting for calibration residual is provided by MicMac ($\rho = 0.6$) and *GSD* varies according to the image pair with an average value of 20 m (Table 1). Due to our singular configuration, the flying height and the stereo base vary a lot between two shots so the p/h ratio was calculated with the emission angles. This formula is actually more satisfying because it provides *EP* for each pixel of the DTM (Figure 10), as the emission angle varies into the images accounting for the distance between the ground and the sensor (see supporting information Figure S3).

The expected vertical precision map shows the regions where the geometry of acquisition does not allow a precise intersection of the rays (EP is high, Figure 10). These regions unsurprisingly correspond to areas where the correlation is low (Figure 9), except for isolated spots that we decided to exclude from the DTM due to low confidence (Figure 7). We also masked pixels with a correlation score lower than 0.5, the reference threshold used in MicMac (in SOCET SET, it equals 0.4, as documented in the source code and the user guide). The resulting mask is applied to Figures 9 and 10.

Nevertheless, despite these adjustments, the resulting IPGP-DTM presents a global tilt of ~9.5° (measured in Figure 11a, see supporting information Figure S5), which leads to an improbable configuration: The dark lakebed is higher than the bright hills (Karkoschka & Schröder, 2016; Perron et al., 2006; Tomasko et al., 2005) and the rivers, the mouth of which is located in the dark lowlands, rise up the slope. This overall inclination is due to improperly addressed photogrammetric problems. Indeed, an intrinsic mathematical

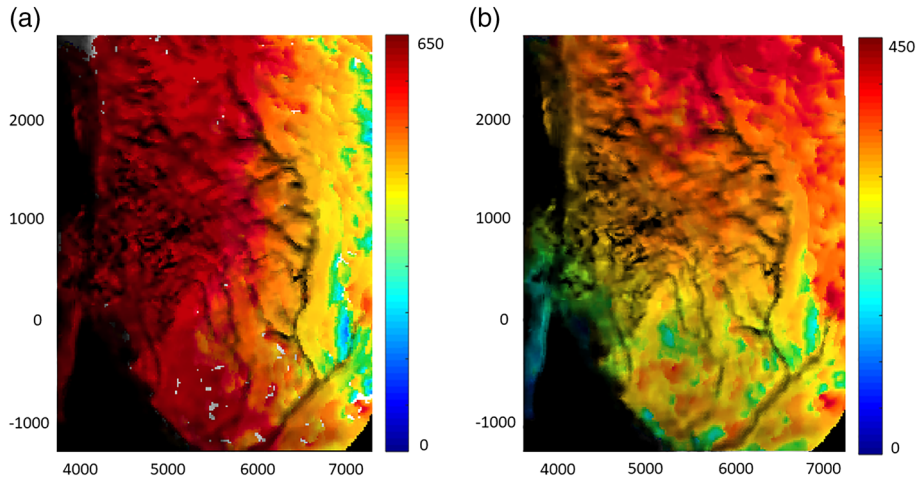

Figure 11. (a) DTM resulting from MicMac reconstruction (global tilt of about 9.5°). (b) Same DTM after a rotation of −10° along the *y* axis and 3° along the *x* axis. Both DTM are superimposed on their corresponding orthorectified mosaics (with transparency). White and neutral gray patches on (a) are due to NoData values in the DTM (due to masking process) that take the color of the superimposed orthoimage (they do not appear in panel b because these values have been reinterpolated during the rotation process). Color bars show the DTM elevations (in meters) and the coordinates (in meters) are in a local tangent frame.

indeterminacy affects the global orientation of the IPGP-DTM plane. A reason is the nonoptimal positions and orientations of the DISR cameras at the acquisition time and by the alignment of the GCP (Figure 7). Note that the global tilt of the IPGP-DTM does not affect the high-frequency topography (i.e., the relative local slopes). Thus, it is necessary to find an alternative method to solve for the global inclination of the scene, independent of the photogrammetric reconstruction software.

3.3. Determination of the IPGP-DTM Tilt

The last step of the workflow consists in finding the overall inclination of the IPGP-DTM. As no other topographic data derived from the Cassini mission can help constrain the global tilt of the IPGP-DTM, a new strategy should be adopted. The USGS scientists fixed this problem by setting the elevation of lakebed in the USGS-DTM to 0, assuming that there is no global slope. To avoid making any prior assumption concerning the global inclination, we determined the tilt using morphological information and river routing. Routing is commonly used in hydrology to determine the natural route taken by a liquid over a given topography. Ideally, a liquid flowing on the IPGP-DTM should choose the same path as the one followed by the rivers seen in the images. Thus, the idea is to compare this routing with the actual location of the rivers (Burr et al., 2013; Perron et al., 2006; L. A. Soderblom, Tomasko, et al., 2007; Tomasko et al., 2005). The tilt corresponding to the best match will be considered as the optimal one. This original method is completely new and has been developed for this particular study. Nevertheless, it could be apply to any case where there is a lack of GCP as long as the DTM includes rivers (or other morphological features bringing external constraints).

We considered that the flow path remained unchanged and that the rivers should flow downhill. Note that we can reasonably consider that the formation of the landscape in this region is due to recent erosion with little to no contribution from uplift. Indeed, during the 13 years of the mission, the Cassini spacecraft has observed two superstorms at the equator (Turtle et al., 2011). Their large extent (more than 500,000 km^2) and the proximity of one of them to the Huygens landing site (about nearly 50° to the west) sign that recent rains may occur in this region.

The strategy therefore consists in (i) rotating the IPGP-DTM produced with MicMac along the *x* axis and *y* axis, from −20° to +20° with a 1° step, (ii) calculating the routing using the Matlab TopoToolBox (Schwanghart & Scherler, 2014; Tarboton, 1997), and (iii) comparing it to a river mask produced using the orthorectified mosaic (Figure 7). To minimize misinterpretation, three masks were manually drawn by different operators, and we kept their intersection as the final one. For this comparison, we only focused on the major rivers to the right of the scene (outlined in red in Figure 7), leaving aside the shorter and stubbier rivers to the left that are not discernible enough.

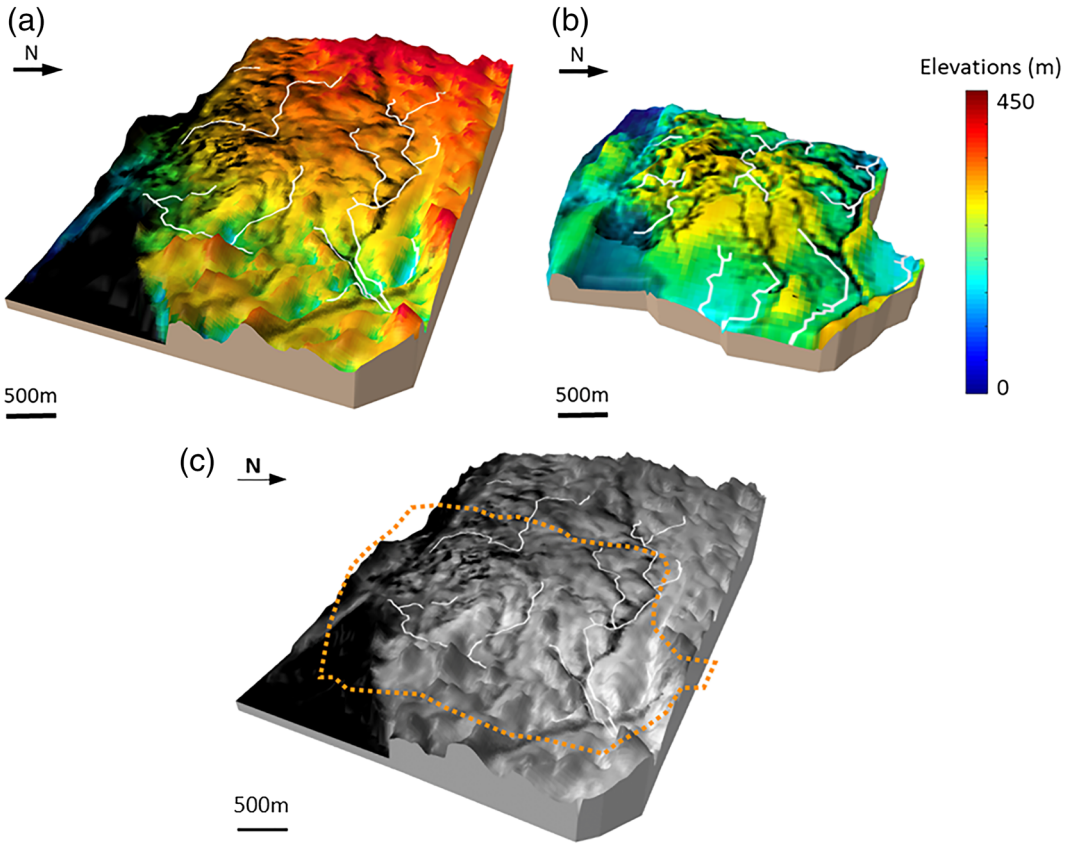

Figure 12. Three-dimensional views of the DTM: (a) IPGP-DTM (see also supporting information Figure S7), (b) USGS-DTM, and (c) IPGP-DTM with the footprint of the USGS-DTM (orange dashes). The vertical exaggeration is 1.5. The routing is superimposed (white line) on each DTM.

The routing algorithm computes the flow direction according to a single angle taken as the steepest downward slope on the eight triangular facets centered at pixel of the IPGP-DTM (Tarboton, 1997). It also calculates the "upslope area" contributing to each pixel. It has the disadvantage of draining the fluid into all the cells downstream of a slope, regardless of the slope inclination. In this way, the noise in the IPGP-DTM, which can cause unrealistic altitude fluctuations, is treated as local minima by the routing algorithm and can generate unrealistic flow routing. It is thus important to establish a minimum threshold on the routing to ensure that fluids do not accumulate in these noisy regions and flow in a more realistic way. This can be done by identifying an area of the DTM where the routing algorithm leads to fluid accumulation when no rivers are observed and by computing a threshold on the drainage area (i.e., a minimum number of drained cells) that allows to eliminate these unrealistic fluid accumulations. Then we apply it to the whole topography.

For each pair of rotation angles, a matching score is calculated as the percentage of pixels determined by routing that match the actual rivers (Figure 12). The maximum score is 62%, for an optimal rotation angle of $-10°$ along the y axis and $3°$ along the x axis (see supporting information Figure S6). Interestingly, it amounts to bringing the IPGP-DTM back close to horizontal, with only a remaining gentle global slope and rivers going down the slope. Nevertheless, this score should be interpreted carefully: It does not mean that 62% of the rivers has been rebuilt with the new IPGP-DTM. Indeed, the shorter and stubbier rivers were not taken into account for this calculation, and the network calculated by the routing does not always follow the rivers continuously.

4. Results and Discussion

The overall inclination and shape of the IPGP-DTM are consistent with the expected direction of the flow (L. A. Soderblom, Tomasko, et al., 2007). This is proved by the routing where the large rivers flow from the bright zone toward the dark area. Note that the small rivers to the left of the scene, which were excluded

from the score calculation, also flow in the right direction from the highlands to the riverbed (see Figure 12 and supporting information Figure S7).

However, some areas display a suspicious morphology. For instance the edges of the IPGP-DTM, which we did not mask because of high correlation scores, are very steep. Since such slopes (up to 80°) are not observed on Earth at such small scales, the accuracy of the IPGP-DTM in these regions is questionable. Moreover, the routing does not well match the rivers in these regions that display the highest EP values, in particular the region for $y < 0$, which is 2 to 3 times higher than in the center of the DTM (Figure 10). As a consequence, we advise users to always refer to the EP map when using the IPGP-DTM.

The first improvement of the IPGP-DTM concerns the size of the reconstructed region, which is larger than the USGS-DTM (10.3 km^2 vs. 7.5 km^2) because we used more images. The horizontal sampling of the IPGP-DTM is also better (18 m/px vs. 50 m/px).

The flow direction on the topography of both DTM was calculated in the same way using the TopoToolBox routine. Since they do not have the same size and resolution, we cannot apply the same threshold for routing, nevertheless we applied the same method to determine it. The resulting matching score is 35% if we compute it on the original USGS-DTM (L. A. Soderblom, Tomasko, et al., 2007). It is worth noting that, since the orientation of the USGS-DTM was manually clipped to 0, we tried to find out if we could find an optimal orientation as we did for the IPGP-DTM. Therefore, we rotated the USGS-DTM in order to find the best matching score, as done with the IPGP-DTM, and found a score of 56%. This score correspond to a rotation angle of 4° along the y axis and 3° along the x axis, which means that the global slope was underestimated, and by slightly tilting the USGS-DTM, we find a more coherent configuration with regard to the shape and location of the routing (see supporting information Figure S8). However, with this rotation, the land at the bottom right of Figure S4 is at the same elevation as the lakebed at the bottom left, which is questionable.

If we consider the original USGS-DTM (no inclination) used in previous studies (Jaumann et al., 2008; Tewelde et al., 2013; Tomasko et al., 2005), the routing shapes calculated from the two DTM are very different. The USGS-DTM provides a radial shape routing, while the IPGP-DTM provides a rather dendritic or rectangular shape. According to the literature (Burr et al., 2013; Perron et al., 2006) and even by simple visual inspection, the networks observed in our region of interest have dendritic or rectangular shapes. As a consequence the IPGP-DTM seems to provide a better representation of the local topography.

The last comparison consists in analyzing several river profiles and transects/cross sections in order to check if the inclination of the rivers is consistent with the theoretical direction of flow and if the rivers, carved by liquid hydrocarbons, form depressions. As far as the cross sections are concerned, the river bottoms are generally located on flat areas or in depressions for both DTM, except in a few cases where the rivers are located on slopes (Figure 13). However, it is worth to note that, due to a coarser resolution, the USGS-DTM has only one manual measurement point per river transect compared to an average of three points for the IPGP-DTM. As for the river profiles, the flow of the main river (Profile C-C' in green in Figure 13) follows the expected flow direction in the case of the IPGP-DTM as opposed to the USGS-DTM, where the channel flows in the wrong direction.

5. Conclusion

New investigation of the topography around the Huygens landing site has been successfully carried out. We developed a new strategy that could overcome the high complexity of the data set, unusual even for planetary data, and provided a fully documented and reproducible workflow. This procedure could be apply in situations with such a complex data set. For instance, it could be applied both to poorly known and hard-to-reach terrestrial areas (i.e., Antarctica) and to archive data from former planetary missions (i.e., Voyager and Galileo). Besides a new strategy, the article provides a new DTM with a higher spatial sampling and a more reliable topography since it is much less interpolated than the previous product. This DTM offers new opportunities for investigating the topography of fluvial landscape at Titan's equatorial region with an unprecedented resolution. It could bring new insights on Titan's landscape formation mechanisms by quantitatively characterizing the morphometry of these rivers and the topography of their associated drainage basins.

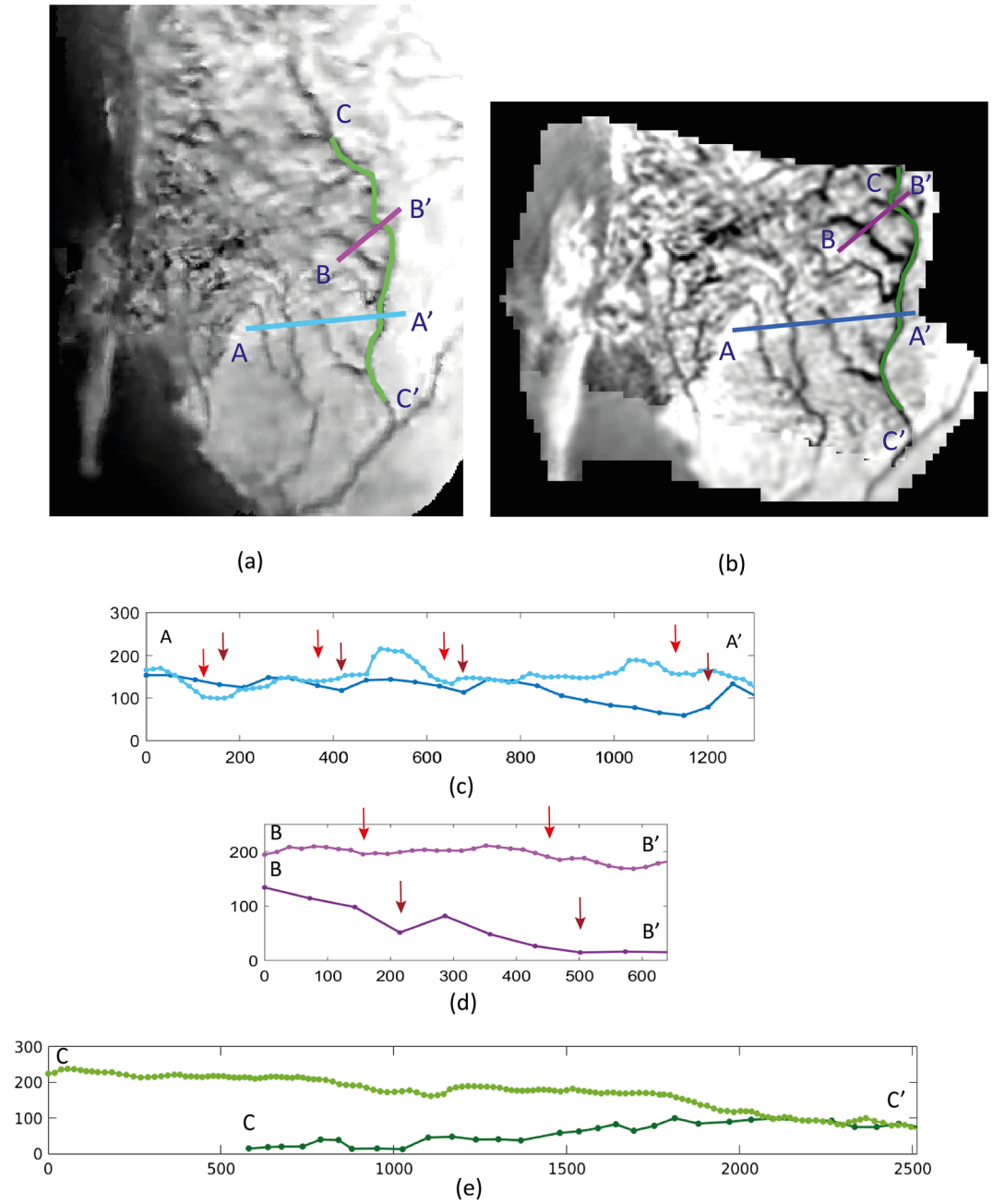

Figure 13. Orthorectified mosaics calculated from (a) the IPGP-DTM and (b) the USGS-DTM. We display two cross-sectional profiles (c and d) and a profile along a river (e). The horizontal axis of the graphs represents the length of the transect and the vertical axis represents the altitude (in meters). The darker colors in each graph represent the cross sections and follow-ups of the USGS-DTM, while the lighter colors correspond to those of the IPGP-DTM. The dark red arrows refer to the valley bottoms visible on the orthorectified mosaics of USGS-DTM, and the light red arrows correspond to those of our orthorectified mosaics. The two orthorectified images (and therefore the arrows) are offset because the topography of the two DTMs are not identical.

Appendix A: Local Tangent Plane definition

The local tangent plane (LTP) is an orthogonal, rectangular, reference system, the origin of which is defined at an arbitrary point on the planet surface (here we took the nadir of the Image #450 located at (167.64370°E, −10.577749°N)). Among the three coordinates one represents the position along the northern axis, one along the local eastern axis, and the last one is the vertical position. If (λ, ϕ, h) are the coordinates of a given point

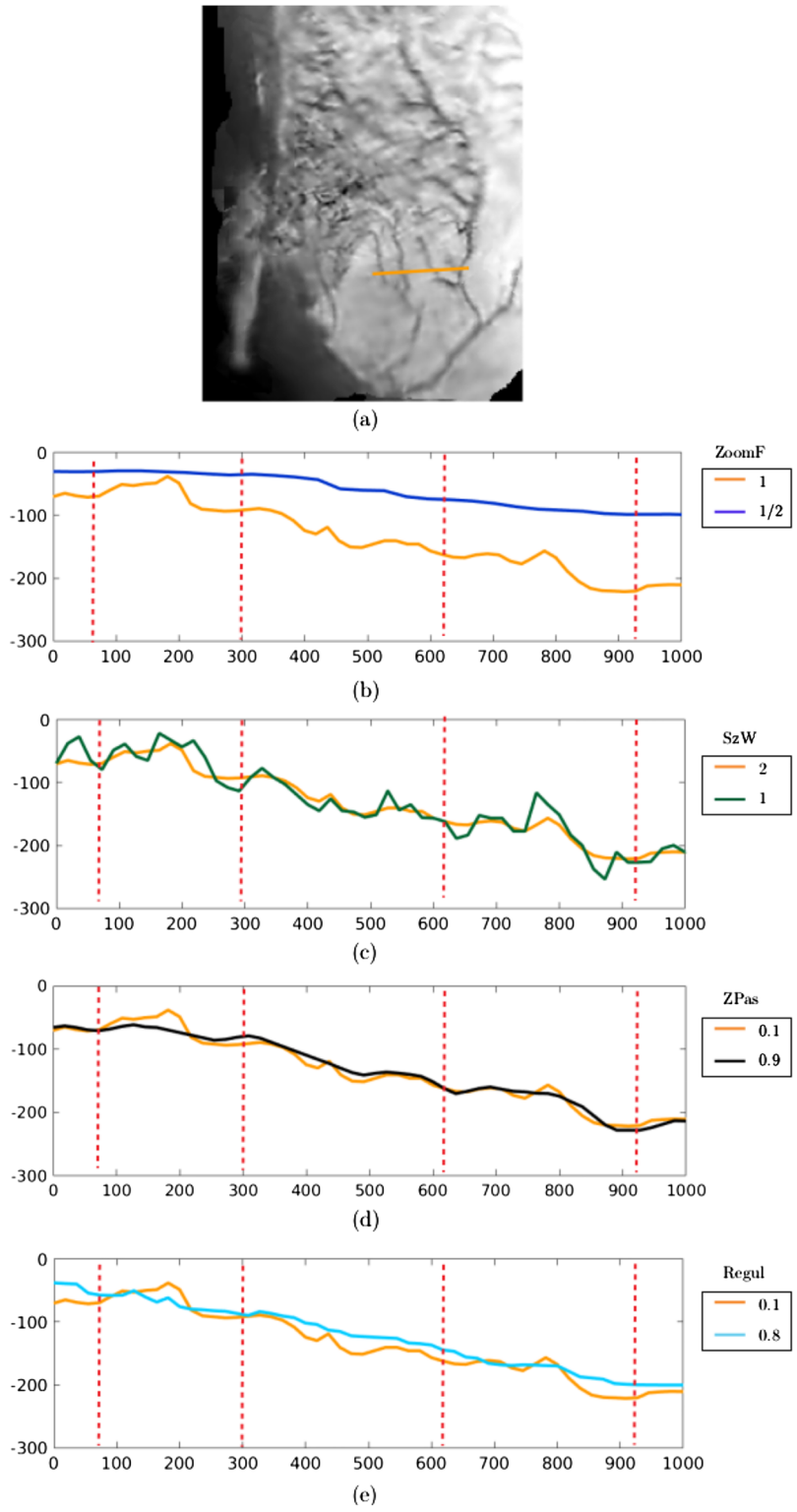

Figure B1. (a) Orthorectified mosaic calculated from the IPGP-DTM. We display the cross-sectional profile of the river (in orange on the orthoimage) and change the value of each parameters for each panel. On every plot, the orange line represent the profile of the final DTM, and the other line is the profile of the DTM with a different parameter (the unit for both axes is the meter). (b) The dark blue line is the profile of the DTM for a smaller final resolution value, (c) the dark green plot for a smaller size correlation window, (d) the dark line correspond to a higher quantification step, and (e) the blue plot is for a larger regularization factor. The dashed red line refers to the valley bottoms visible on the orthorectified mosaics of DTM.

in the geographical frame, the coordinates (x_t,y_t,z_t) of the LTP are defined as follows:

$$\begin{pmatrix} x_t \\ y_t \\ z_t \end{pmatrix} = \begin{pmatrix} -sin(\phi) & cos(\phi) & 0 \\ -cos(\phi)sin(\lambda) & -sin(\lambda)sin(\phi) & cos(\lambda) \\ cos(\lambda)cos(\phi) & cos(\lambda)sin(\phi) & sin(\lambda) \end{pmatrix} \cdot \begin{pmatrix} x - x_0 \\ y - y_0 \\ z - z_0 \end{pmatrix}$$

with:

- (x,y,z) the Cartesian coordinates of the given point
- (x_0,y_0,z_0) the Cartesian coordinates of our reference point

Appendix B: Dense Pixel Matching Parameters

A sensitivity analysis has been performed on all the parameters of the dense pixel matching step. The parameters selection was done manually, by changing their value in order to keep most of the details while reducing the noise level. As observed on the Figure B1, a smaller final resolution and a bigger quantification step and regularization factor tend to smooth the DTM and cannot detect the bottom of the rivers. On the contrary, a smaller size of correlation window tends to noise the DTM.

Data Availability Statement

MicMac software can be downloaded for free (https://micmac.ensg.eu/index.php/Accueil), and the SPICE kernels are publicly available (https://doi.org/10.5270/esa-ssem3np). The DTM and other products resulting from this work are available online (https://doi.org/10.5270/esa-3uja374).

Acknowledgments
The authors thank Chuck See for providing the reprocessed DISR images. They also thank the reviewers for their valuable comments and advice.

References

Aharonson, O., Hayes, A. G., Lopes, R., Lucas, A., Hayne, P., & Perron, J. T. (2014). *Titan: Surface, atmosphere and magnetosphere* (pp. 43–75). Cambridge: Cambridge University Press.

Archinal, B. A., Tomasko, M. G., Rizk, B., Soderblom, L. A., Kirk, R. L., Howington-Kraus, E., et al. (2006). Photogrammetric analysis of Huygens DISR images of Titan. ISPRS.

Atreya, S. K., Adams, E. Y., Niemann, H. B., Demick-Montelara, J. E., Owen, T. C., Fulchignoni, M., et al. (2006). Titan's methane cycle. *Planetary and Space Science*, *54*(12), 1177–1187.

Barnes, J. W., Brown, R. H., Soderblom, L. A., Buratti, B. J., Sotin, C., Rodriguez, S., et al. (2007b). Global-scale surface spectral variations on Titan seen from Cassini/VIMS. *Icarus*, *186*(1), 242–258.

Barnes, J. W., Brown, R. H., Soderblom, L. A., Sotin, C., Le Mouèlic, S., Rodriguez, S., et al. (2008). Spectroscopy, morphometry, and photoclinometry of Titan's dunefields from Cassini/VIMS. *Icarus*, *195*(1), 400–414.

Barnes, J. W., Radebaugh, J., Brown, R. H., Wall, S., Soderblom, L. A., Lunine, J., et al. (2007). Near-infrared spectral mapping of Titan's mountains and channels. *Journal of Geophysical Research*, *112*, E11006. https://doi.org/10.1029/2007JE002932

Black, B. A., Perron, J. T., Burr, D. M., & Drummond, S. A. (2012). Estimating erosional exhumation on Titan from drainage network morphology. *Journal of Geophysical Research*, *117*, E08006. https://doi.org/10.1029/2012JE004085

Bretar, F., Arab-Sedze, M., Champion, J., Pierrot-Deseilligny, M., Heggy, E., & Jacquemoud, S. (2013). An advanced photogrammetric method to measure surface roughness: Application to volcanic terrains in the Piton de la Fournaise, Reunion Island. *Remote Sensing of Environment*, *135*, 1–11.

Brossier, J. F., Rodriguez, S., Cornet, T., Lucas, A., Radebaugh, J., Maltagliati, L., et al. (2018). Geological evolution of Titan's equatorial regions: Possible nature and origin of the dune material. *Journal of Geophysical Research: Planets*, *123*, 1089–1112. https://doi.org/10.1029/2017JE005399

Burr, D. M., Emery, J. P., Lorenz, R. D., Collins, G. C., & Carling, P. A. (2006). Sediment transport by liquid surficial flow: Application to Titan. *Icarus*, *181*(1), 235–242.

Burr, D. M., Perron, J. T., Lamb, M. P., Irwin III, R. P., Collins, G. C., Howard, A. D., & Drummond, S. A. (2013). Fluvial features on Titan: Insights from morphology and modeling. *GSA Bulletin*, *125*(3-4), 299–321.

Charles, H. A. (1996). Ancillary data services of NASA's navigation and ancillary information facility. *Planetary and Space Science*, *44*(1), 65–70. https://doi.org/10.1016/0032-0633(95)00107-7

Collins, G. C. (2005). Relative rates of fluvial bedrock incision on Titan and Earth. *Geophysical Research Letters*, *32*, L22202. https://doi.org/10.1029/2005GL024551

Cornet, T., Bourgeois, O., Le Moulic, S., Rodriguez, S., Lopez Gonzalez, T., Sotin, C., et al. (2012). Geomorphological significance of ontario lacus on Titan: Integrated interpretation of Cassini VIMS, ISS and RADAR data and comparison with the Etosha Pan (Namibia). *Icarus*, *218*(2), 788–806.

ESA SPICE Service (2019). Huygens Operational SPICE kernel dataset.

Galand, M., Yelle, R., Cui, J., Wahlund, J.-E., Vuitton, V., Wellbrock, A., & Coates, A. (2010). Ionization sources in Titan's deep ionosphere. *Journal of Geophysical Research*, *115*, A07312. https://doi.org/10.1029/2009JA015100

Hayes, A. G., Aharonson, O., Callahan, P., Elachi, C., Gim, Y., Kirk, R., et al. (2008). Hydrocarbon lakes on Titan: Distribution and interaction with a porous regolith. *Geophysical Research Letters*, *35*, L09204. https://doi.org/10.1029/2008GL033409

Hayes, A. G., Lorenz, R. D., & Lunine, J. I. (2018). A post-Cassini view of Titan's methane-based hydrologic cycle. *Nature Geoscience*, *11*(5), 306–313.

Jaumann, R., Brown, R. H., Stephan, K., Barnes, J. W., Soderblom, L. A., Sotin, C., et al. (2008). Fluvial erosion and post-erosional processes on Titan. *Icarus*, *197*(2), 526–538.

Karkoschka, E. (2016). Titan's meridional wind profile and Huygens orientation and swing inferred from the geometry of DISR imaging. *Icarus*, *270*, 326–338. Titan's Surface and Atmosphere.

Karkoschka, E., & Schröder, S. E. (2016). The DISR imaging mosaic of Titan's surface and its dependence on emission angle. *Icarus*, *270*, 307–325. Titan's Surface and Atmosphere.

Karkoschka, E., Tomasko, M. G., Doose, L. R., See, C., McFarlane, E. A., Schrder, S. E., & Rizk, B. (2007). Disr imaging and the geometry of the descent of the huygens probe within Titan's atmosphere. *Planetary and Space Science*, *55*(13), 1896–1935. Titan as seen from Huygens.

Kazeminejad, B., & Atkinson, D. H. (2004). The ESA huygens probe entry and descent trajectory reconstruction. In *Planetary probe atmospheric entry and descent trajectory analysis and science*, *544*, pp. 137–149.

Kazeminejad, B., Atkinson, D. H., & Lebreton, J.-P. (2011). Titan's new pole: Implications for the Huygens entry and descent trajectory and landing coordinates. *Advances in Space Research*, *47*(9), 1622–1632.

Keller, H. U., Grieger, B., Kppers, M., Schrder, S. E., Skorov, Y. V., & Tomasko, M. G. (2008). The properties of Titan's surface at the huygens landing site from DISR observations. *Planetary and Space Science*, *56*(5), 728–752. Titan as seen from Huygens - Part 2.

Kirk, R. L., Howington Kraus, E., Redding, B., Galuszka, D., Hare, T. M., Archinal, B. A., et al. (2003). High-resolution topomapping of candidate MER landing sites with Mars Orbiter Camera narrow-angle images. *Journal of Geophysical Research*, *108*(E12), 8088.

Langhans, M. H., Jaumann, R., Stephan, K., Brown, R. H., Buratti, B. J., Clark, R. N., et al. (2012). Titan's fluvial valleys: Morphology, distribution, and spectral properties. *Planetary and Space Science*, *60*(1), 34–51. Titan Through Time: A Workshop on Titan's Formation, Evolution and Fate.

Lebreton, J.-P., Witasse, O., Sollazzo, C., Blancquaert, T., Couzin, P., Schipper, A.-M., et al. (2005). An overview of the descent and landing of the Huygens probe on Titan. *Nature*, *438*(7069), 1476–4687.

Lopes, R. M. C., Malaska, M. J., Solomonidou, A., Le Gall, A., Janssen, M. A., Neish, C. D., et al. (2016). Nature, distribution, and origin of Titan's undifferentiated plains. *Icarus*, *270*, 162–182.

Lopes, R. M. C., Mitchell, K. L., Wall, S. D., Mitri, G., Janssen, M., Ostro, S., et al. (2007). The lakes and seas of Titan. *Eos, Transactions American Geophysical Union*, *88*(51), 569–570.

Lorenz, R. D., Lopes, R. M., Paganelli, F., Lunine, J. I., Kirk, R. L., Mitchell, K. L., et al. (2008). Fluvial channels on Titan: Initial Cassini radar observations. *Planetary and Space Science*, *56*(8), 1132–1144.

Lorenz, R. D., & Lunine, J. I. (1996). Erosion on Titan: Past and present. *Icarus*, *122*(1), 79–91.

Lorenz, R. D., Wall, S., Radebaugh, J., Boubin, G., Reffet, E., Janssen, M., et al. (2006). The sand seas of Titan: Cassini radar observations of longitudinal dunes. *Science*, *312*(5774), 724–727.

Lorenz, R. D., Wood, C. A., Lunine, J. I., Wall, S. D., Lopes, R. M., Mitchell, K. L., et al. (2007). Titan's young surface: Initial impact crater survey by cassini radar and model comparison. *Geophysical Research Letters*, *34*, L07204. https://doi.org/10.1029/2006GL028971

Lowe, D. G. (2004). Distinctive image features from scale-invariant keypoints. *International Journal of Computer Vision*, *60*(2), 91–110.

Lunine, J. I., & Atreya, S. K. (2008). The methane cycle on Titan. *Nature*, *1*(159).

Perron, J. T., Lamb, M. P., Koven, C. D., Fung, I. Y., Yager, E., & Ádámkovics, M. (2006). Valley formation and methane precipitation rates on Titan. *Journal of Geophysical Research*, *111*, E11001. https://doi.org/10.1029/2005JE002602

Pierrot-Deseilligny, M., & Clery, I. (2011). APERO, an open source bundle adjusment software for automatic calibration and orientation of set of images. *International Archives of the Photogrammetry, Remote Sensing and Spatial Information Sciences*, *XXXVIII-5*, 269–276.

Pierrot-Deseilligny, M., & Paparoditis, N. (2006). A multiresolution and optimization-based image matching approach: An application to surface reconstruction from SPOT5-HRS stereo imagery. ISPRS Workshop on Topographic Mapping from Space (With Special Emphasis on Small Satellites, 15.

Porco, C. C., Baker, E., Barbara, J., Beurle, K., Brahic, A., Burns, J. A., et al. (2005). Imaging of Titan from the Cassini spacecraft. *Nature*, *434*(7030), 159. https://10.1038/nature03436

Radebaugh, J., Lorenz, R. D., Kirk, R. L., Lunine, J. I., Stofan, E., Lopes, R., Wall, S., & The Cassini Radar Team (2007). Mountains on Titan from Cassini radar. *Icarus*, *192*, 77–91.

Radebaugh, J., Lorenz, R. D., Lunine, J. I., Wall, S. D., Boubin, G., Reffet, E., et al. The Cassini Radar Team (2008). Dunes on Titan observed by Cassini radar. *Icarus*, *194*(2), 690–703.

Rodriguez, S., Garcia, A., Lucas, A., Appr, T., Le Gall, A., Reffet, E., et al. (2014). Global mapping and characterization of Titan's dune fields with Cassini: Correlation between radar and VIMS observations. *Icarus*, *230*, 168–179.

Rodriguez, S., Le Moulic, S., Sotin, C., Clnet, H., Clark, R. N., Buratti, B., et al. (2006). Cassini/VIMS hyperspectral observations of the huygens landing site on Titan. *Planetary and Space Science*, *54*(15), 1510–1523.

Rosu, A.-M., Pierrot-Deseilligny, M., Delorme, A., Binet, R., & Klinger, Y. (2015). Measurement of ground displacement from optical satellite image correlation using the free open-source software MicMac. *ISPRS Journal of Photogrammetry and Remote Sensing*, *100*, 48–59.

Schwanghart, W., & Scherler, D. (2014). TopoToolbox 2 MATLAB-based software for topographic analysis and modeling in Earth surface sciences. *Earth Surface Dynamics*, *2*, 1–7.

Soderblom, J. M., Brown, R. H., Soderblom, L. A., Barnes, J. W., Jaumann, R., Le Mouélic, S., et al. (2010). Geology of the selk crater region on Titan from Cassini VIMS observations. *Icarus*, *208*(2), 905–912.

Soderblom, L. A., Kirk, R. L., Lunine, J. I., Anderson, J. A., Baines, K. H., Barnes, J., et al. Cassini Vims Team, Cassini Radar Team, & Huygens Disr Team (2007). Correlations between Cassini VIMS spectra and RADAR SAR images: Implications for Titan's surface composition and the caractere of the Huygens probe landing Site. *Planetary and Space Science*, *55*, 2025–2036.

Soderblom, L. A., Tomasko, M. G., Archinal, B. A., Becker, T. L., Bushroe, M. W., Cook, D. A., et al. (2007). Topography and geomorphology of the Huygens landing site on Titan. *Planetary and Space Science*, *55*(13), 2015–2024.

Stofan, E. R., Elachi, C., Lunine, J. I., Lorenz, R. D., Stiles, B., Mitchell, K. L., et al. (2007). The lakes of Titan. *Nature*, *445*(7123), 61–64. https://doi.org/10.1038/nature05438

Tarboton, D. G. (1997). A new method for the determination of flow directions and upslope areas in grid digital elevation models. *Water Resources Research*, *33*(2), 309–319.

Tewelde, Y., Perron, J. T., Ford, P., Miller, S., & Black, B. (2013). Estimates of fluvial erosion on Titan from sinuosity of lake shorelines. *Journal of Geophysical Research: Planets*, *118*, 2198–2212. https://doi.org/10.1002/jgre.20153

Tomasko, M. G., Archinal, B., Becker, T., Bézard, B., Bushroe, M., Combes, M., et al. (2005). Rain, winds and haze during the Huygens probe's descent to Titan's surface. *Nature*, *438*(7069), 765–778.

Tomasko, M. G., Buchhauser, D., Bushroe, M., Dafoe, L. E., Doose, L. R., Eibl, A., et al. (2002). The Descent Imager/Spectral Radiometer (DISR) experiment on the huygens entry probe of Titan. *Space Science Reviews*, *104*, 469–551.

Tomasko, M. G., Buchhauser, D., Bushroe, M., Dafoe, L. E., Doose, L. R., Eibl, A., et al. (2003). The Descent Imager/Spectral Radiometer (DISR) experiment on the huygens entry probe of Titan. In Russell C. T. (Ed.), *The Cassini-Huygens mission* pp. 469–551). Dordrecht: Springer.

Triggs, B., McLauchlan, P. F., Hartley, R. I., & Fitzgibbon, A. W. (1999). Bundle adjustment a modern synthesis. In *International workshop on vision algorithms*, Springer, pp. 298–372.

Turtle, E. P., Perry, J. E., Hayes, A. G., Lorenz, R. D., Barnes, J. W., McEwen, A. S., et al. (2011). Rapid and extensive surface changes near Titan's equator: Evidence of April showers. *Science*, *331*(6023), 1414–1417. https://science.sciencemag.org/content/331/6023/1414

Yung, Y. L., Allen, M., & Pinto, J. P. (1984). Photochemistry of the atmosphere of Titan—Comparison between model and observations. *Astrophysical Journal Supplement Series*, *55*, 465–506.